Title: Co-opted transposons help perpetuate conserved higher-order chromosomal structures

Short title: Co-opted TEs maintain conserved 3D genome

One-sentence summary: Co-option of transposable elements maintains conserved 3D genome structures via CTCF binding site turnover in human and mouse.

Authors: Mayank NK Choudhary[1], Ryan Z Friedman[1], Julia T Wang[1], Hyo Sik Jang[1], Xiaoyu Zhuo PhD[1], Ting Wang PhD[1,*]

Affiliations: [1]The Edison Family Center for Genome Sciences & Systems Biology, Department of Genetics, Washington University, St. Louis, MO

[*]Corresponding author:
Ting Wang, PhD, Department of Genetics,
Washington University School of Medicine, 4515 McKinley Avenue
Campus Box 8510
St. Louis, MO 63110, USA.
Phone: (314) 286-0865
E-mail address: twang@genetics.wustl.edu

3782 Words
0 Table
4 Figures

ABSTRACT (227 words)

Transposable elements (TEs) make up half of mammalian genomes and shape genome regulation by harboring binding sites for regulatory factors. These include architectural proteins—such as CTCF, RAD21 and SMC3—that are involved in tethering chromatin loops and marking domain boundaries. The 3D organization of the mammalian genome is intimately linked to its function and is remarkably conserved. However, the mechanisms by which these structural intricacies emerge and evolve have not been thoroughly probed. Here we show that TEs contribute extensively to both the formation of species-specific loops in humans and mice via deposition of novel anchoring motifs, as well as to the maintenance of conserved loops across both species via CTCF binding site turnover. The latter function demonstrates the ability of TEs to contribute to genome plasticity and reinforce conserved genome architecture as redundant loop anchors. Deleting such candidate TEs in human cells leads to a collapse of such conserved loop and domain structures. These TEs are also marked by reduced DNA methylation and bear mutational signatures of hypomethylation through evolutionary time. TEs have long been considered a source of genetic innovation; by examining their contribution to genome topology, we show that TEs can contribute to regulatory plasticity by inducing redundancy and potentiating genetic drift locally while conserving genome architecture globally, revealing a paradigm for defining regulatory conservation in the noncoding genome beyond classic sequence-level conservation.

Keywords: 3D genome, loops, evolution, conservation, transposable elements, binding site turnover

46 **BACKGROUND**

47 The 3D organization of various genomes has been mapped at high resolution using a
48 variety of methods (*1-5*). While genome folding is largely conserved in mammals (*1,4*), the
49 genetic forces shaping its emergence and evolution remain poorly understood. Two distinct
50 yet mutually non-exclusive models (*6*) have recently gained much traction: that of phase
51 separation (*7*) and of loop extrusion (*8,9*) by factors such as CTCF. In relation to the latter, TEs
52 are known to contain and disseminate functional regulatory sequences (*10-13*) including that of
53 CTCF. In contrast to relying on point mutations to evolve a functional CTCF binding site, TE
54 transposition presents an attractive model for rapid regulatory sequence dissemination and
55 regime building (*14-17*). Hence, we hypothesized that TEs have been a rich source of sequence
56 for the assembly and tinkering of higher-order chromosomal structures. We studied the
57 influence of all repetitive elements (REs) in establishing higher-order chromosomal structures
58 and, more specifically, the role of TEs in the evolution of these higher-order chromosomal
59 structures in humans and mice.

60

61 **RESULTS**

62 We examined REs' contribution to loop anchor CTCF sites using published genome-
63 wide chromosomal conformation capture data from assays including ChIA-PET (*2*) and Hi-C in
64 human (GM12878, HeLa, HMEC, IMR90, K562, NHEK) and mouse (ESCs, NSCs, CH12-LX) cell
65 lines (*1*). We determined that 398 out of 3159 (12.6%) unique loop anchor CTCF sites were
66 derived from REs in the mouse lymphoblastoid cell line. These RE-derived CTCF sites help
67 establish 451 out of 2718 (16.6%) loops with discernible, unique CTCF loop anchors (Fig 1A, B).
68 In the corresponding human lymphoblastoid cell line, REs contributed 935 out of 8324 (11.2%)
69 unique loop anchor CTCF sites that help establish 1244 out of 8007 (15.6%) loops. Overall, REs
70 contributed 9-15% of the anchor CTCF sites that result in 12-18% loops in humans and 12-23%
71 of the anchor CTCF sites that result in 15-27% loops in mouse, across a variety of cell lines (Fig
72 1A, B).

73 In both species, RE-derived loop anchor CTCF sites were largely derived from TEs
74 (>95%) and their class of origin (SINE, LINE, LTR, DNA) showed a species-biased distribution

75 (Fig 1C). Using the highest resolution *in-situ* HiC maps in matched lymphoblastoid cell types in
76 mice (CH12-LX) and humans (GM12878), we compared the composition of the RE-derived loop
77 anchor CTCF sites. While the mouse lineage was profoundly shaped by the SINEs (70%, 4x
78 enrichment over background), the human lineage was overrepresented by retroviral LTR
79 elements and DNA transposons (36% and 22%, 2x and 3x enriched over the background
80 respectively) (Fig 1D). At the family level, the B2 SINEs in mice were 13-fold enriched over
81 background and contributed 65% of TE-derived loop anchor CTCF sites. In humans, the hAT-
82 Charlie family of DNA transposons contributed 13% of TE-derived loop anchor CTCF sites, a 4-
83 fold enrichment over background (Fig 1E). These contributions are underestimates as we have
84 yet to (i) uniquely identify all loop anchor CTCF sites (especially in repetitive regions), and (ii)
85 annotate all repetitive elements, especially ancient TEs that have diverged far from their
86 identity (*18*). Further, we looked at the cell-type specificity of these loop anchor CTCF sites in
87 humans and see that 1334 out of 2017 (66%) RE-derived loop anchor CTCF sites were found in
88 only one cell type (Supplementary Figure 1A). However, we did not find any specific TE family
89 that enriches for cell-type specific loop anchor CTCF sites in the cell lines profiled
90 (Supplementary Figure 1B).

91 To study the evolution of chromatin loops, we compared their conservation
92 (Supplementary Methods) in matched human and mouse cell-types. Briefly, we used the
93 liftOver tool (*19*) to compare loops across species and required exactly one reciprocal match
94 (reciprocal best hit) to designate conserved loops. We found that 48% of all mouse loops (1596
95 out of 3331) had a loop call in the corresponding syntenic region in humans (Table S1.1). Our
96 observation is in close agreement with prior studies (*1,4*) that show about half of all higher-
97 order chromosomal structures to be conserved. We then sought to characterize the
98 contribution of TEs to various classes of loops based on their orthology.

99 We compared the origin of loop anchor CTCF sites of orthologous loops in mouse and
100 human. We found that out of 1596 orthologous loops, 142 (8.9%) in mouse and 108 (6.7%) in
101 human had at least one TE-derived loop anchor CTCF site (Fig 2A). In addition to orthologous
102 loops, TE-derived loop anchor CTCF sites also gave rise to 24% (409 out of 1735) and 15% (1136
103 out of 7852) non-orthologous (species-specific) loops in mouse and humans, respectively (Fig

104 2A), consistent with the appreciable role of TEs in genome innovation (*14-16,20,21*). Overall,
105 the majority of TE-derived loop anchors in mouse were established by a handful of young TE
106 subfamilies (B3, B2_Mm2, B3A, B2_Mm1t) that expanded in the rodent lineage (*22*) (Fig 2B). In
107 contrast, multiple TE subfamilies of varying evolutionary ages contributed diffusely to CTCF
108 loop anchors in humans (Fig 2C). Altogether, TEs in humans contributed to fewer orthologous
109 loops and distributed over more TE subfamilies than in mouse.

110 Intriguingly, 123/142 (87%) TE-derived orthologous loops in mouse were discordant for
111 TEs in humans (Table S1.2). In the sense: while the loops in humans were anchored at the
112 putative ancestral CTCF binding sites, the syntenic ancestral CTCF motifs were largely
113 degraded or deleted in mouse and the loops were now anchored at CTCF sites derived from
114 nearby, co-opted TEs instead. One such example is an orthologous loop at the 5′ end of the
115 Akap8l gene (Fig 2D) maintained in mouse by a MER20 element transposed ~1.5kb upstream
116 of the degraded ancestral motif which was well conserved in most non-rodent mammals
117 (Supplementary Figure 2). The degradation of the ancestral CTCF motif derived from an
118 ancient MIR3 element that is over 147 million-years-old (see *Methods*) incapacitates CTCF
119 binding as evidenced by the CTCF-ChIP track (Fig 2E). In contrast, the younger MER20 element
120 that inserted ~90 million-years ago harbored strong CTCF binding, providing an anchor site to
121 maintain the conserved loop in mouse. Similarly, we find that 89/108 (82%) TE-derived
122 orthologous loops in human GM12878 cells were discordant for TEs in mouse (Table S1.3). We
123 hypothesized that TEs provide redundant CTCF sites and mediated binding site turnover for
124 CTCF contributing to conserved genome folding events between human and mouse.

125 Moreover, the 123 turned-over loops in mouse represent 127 turnover events (4 loops
126 had both loop anchors turned-over) mediated by 124 unique loop anchors (3 turned-over loop
127 anchors tethered 2 loops each). Out of the 124 unique loop anchors, 61 events represent
128 turnover of the left loop anchor and 63 events represent turnover of the right loop. In terms of
129 CTCF motif orientation—for the 61 left loop anchor turnover events, 53 were positive and 8
130 were negative; and for the 63 right loop anchor turnover events, 45 were negative and 18 were
131 positive (Chi-square test, p-value=5.3×10^{-11}). Similarly, in humans the 89 turned-over loops
132 represent 93 turnover events (4 loops had both loop anchors turned-over) were mediated by 84

133 unique loop anchors (1 turned-over loop anchor tethered 3 loops, and 7 loop anchors tethered 2
134 loops each). Out of the 84 unique loop anchors, 43 events represent turnover of the left loop
135 anchor (43 positive orientation CTCF motif and 0 negative orientation CTCF motif), and 41
136 events represent turnover of the right loop (40 positive orientation CTCF motif and 1 negative
137 orientation CTCF motif) (Chi-square test, p-value=3.6×10^{-19}). These results further lend
138 credence to the loop extrusion model (*8*) and suggest that TE exaptation is more likely when
139 the orientation of the inserted TE (and the underlying CTCF motif provided) is compatible with
140 the local loop structure.
141

mm9 CH12-LX (n=124)	Left Loop Anchor	Right Loop Anchor
+ve CTCF motif	53	18
-ve CTCF motif	8	45

142

hg19 GM12878 (n=84)	Left Loop Anchor	Right Loop Anchor
+ve CTCF motif	43	1
-ve CTCF motif	0	40

143

144 Since the mouse genome is replete with repeat-derived CTCF sites (*22*) that could
145 interfere with the targeted study of specific TE candidates, we decided to validate these
146 hypotheses in human cell lines.
147 Here we examine two candidate TEs that maintain conserved higher-order
148 chromosomal structures in humans: one belonging to the L1M3f subfamily of LINEs, and the
149 other belonging to the LTR41 subfamily of endogenous-retrovirus-derived long terminal
150 repeat (LTR). The former TE replaces the function of a lost ancestral CTCF site (Supplementary
151 Figure 3), while the latter is functionally redundant for an ancestral CTCF site still present in
152 humans (Supplementary Figure 4). These two TEs were specifically chosen as they could be
153 unambiguously attributed to the genome folding function (no other CTCF/Cohesin binding site
154 in the vicinity). Using CRISPR-Cas9, we obtained clones of GM12878 cells bearing homozygous
155 deletions of the L1M3f and LTR41 elements, respectively (Supplementary Figure 5, Table S2.4).

156 We then performed HYbrid-Capture on the *in situ* Hi-C library (Hi-C^2) to examine the effect of
157 the TE deletion on the local 3D structure (*8*) (Table S2.1, S2.2, S2.3).
158 The L1M3f-derived CTCF site was positioned at a conserved domain border and
159 anchored three chromatin loops (Supplementary Figure 3). Upon deletion of this L1M3f, the
160 conserved local chromosomal structure collapsed as evidenced by (i) the loss of focal
161 enrichment in the homozygous TE knockout (KO) contact map in comparison to the wild-type
162 (WT) contact map, and (ii) the fusion of two neighboring domains (Hi-C^2 results: Fig 3A, Hi-C
163 results: Supplementary Figure 6). The Virtual 4C plot anchored at the region surrounding the
164 L1M3f element showed three distinct peaks (corresponding to the three loops in the WT cell
165 line), which were lost in the KO (ΔL1M3f) cell line. We also found that cross-domain
166 interactions significantly increased from 8% in WT to 19% in KO cell lines (~2.4x, Welch's t-test
167 p-value<$1.5x10^{-16}$, Table S2.5) across the L1M3f-established domain boundary, a change
168 specific to the targeted domain and not seen in a control domain from a nearby region (Fig 3C).
169 Thus, the L1M3f element is necessary for maintaining the conserved loops and domain
170 boundary in humans. It represents a novel class of binding site turnover (*23-26*) for CTCF
171 leading to conservation in terms of function via establishment of long-range interactions and
172 potentially the underlying gene regulation, but not in primary local sequence.
173 Our second candidate was a species-specific LTR41-derived CTCF site ("c" in Fig 3D, E)
174 that replaced an ancestral CTCF site derived from a much older TE ("d" in Fig 3D, E) of the
175 MER82 subfamily that is conserved in humans and mouse. The ancestral MER82-derived CTCF
176 site was "decommissioned" as the LTR41 insertion (after the primate-rodent split) provided a
177 negative orientation CTCF motif upstream of the MER82 element. Based on the loop extrusion
178 model, the LTR41-derived CTCF motif would be encountered before the MER82-derived CTCF
179 site and hence the ancestral site is mostly decommissioned in present-day human genome as
180 evidenced by the drastically reduced CTCF binding (Supplementary Figure 4B). In the WT
181 contact map, we observed a bright focal enrichment corresponding to CTCF binding sites a-c
182 suggesting a looping interaction. In contrast, there was little focal enrichment corresponding
183 to a-d (Fig 3D, top row). Additionally, in the WT Virtual 4C track anchored on "a", we observed
184 a clear peak corresponding to LTR41 ("c") suggesting an a-c loop (Fig 3E). Upon deletion of

185 LTR41, the conserved loop's anchor is offset to the MER82-derived CTCF site ("d") downstream
186 of the LTR41 as evidenced by the shift in the focal enrichment in the KO contact map (Fig 3D,
187 bottom row) and an increase in the KO Virtual 4C peak corresponding to the MER82-derived
188 CTCF site (i.e., a-d loop) (Fig 3E, Supplementary Figure 7). Upon anchoring the Virtual 4C on a
189 5-kb window containing LTR41 (c), we observed a peak loss at "a" corresponding to the loss of
190 the a-c loop in the KO, an interaction that existed in the WT cells (Fig 3F). With the ~39kb shift
191 of the anchor site, the half-megabase scale chromosomal structure around the anchor region
192 remained largely preserved (Supplementary Figure 4C). Upon deletion of this TE candidate,
193 the local sequence configuration probably resembled that of the pre TE-insertion, ancestral
194 genome. This example therefore illustrates a potential path by which the local 3D genome
195 evolved upon insertion of the LTR41 element as well as the plasticity TEs, like LTR41 and
196 MER82 in this case, can encode in their host genomes by providing redundant CTCF binding
197 sites.

198 These results support the hypothesis that TEs are able to contribute regulatory
199 robustness and strengthen conserved regulatory architecture as redundant or "shadow" loop
200 anchors. The mouse genome that underwent a lineage-specific expansion of SINE B2s (*22*),
201 which carry a CTCF binding motif, is saturated with such events.

202 TEs are typically silenced by host repressive machineries including DNA and histone
203 methylation (*27-29*). However, a small fraction of TEs escape epigenetic silencing and provide
204 functional regulatory elements for the host in a process termed exaptation (*30-33*). Since CTCF
205 is a methylation sensitive chromatin factor and only binds to unmethylated DNA (*34,35*), we
206 examined the DNA methylation levels of loop anchor CTCF sites of orthologous loops
207 (Supplementary Methods). We found that TE-derived CTCF sites were marked by reduced
208 DNA methylation, similar to their non-TE derived genomic counterparts (Fig 4A). To
209 understand the DNA methylation dynamics through evolution, we took advantage of the
210 differential mutation rate of 5-methylcytosine (5mC) to Thymine (T) (*36*). Unmethylated
211 cytosines (C) mutate to T at a lower rate than 5mC; thus, methylated DNA exhibits higher
212 frequency of C to T mutations (*37*). We found that TEs involved in turnover events had a
213 significantly lower frequency of methylation-associated C-to-T and G-to-A mutations

214 compared to an identically sampled background of TEs not involved in looping (1000
215 simulations), but no difference in all other combined substitutions (summarized human results:
216 Fig 4B; full human and mouse results: Supplementary Figure 8, 9, Table S3). These results
217 suggest that TEs providing CTCF turnover were hypomethylated over evolutionary time to
218 maintain their functional role, compared to other TE copies (Fig 4C).
219

220 **DISCUSSION**

221 TEs have substantially contributed to higher order chromatin structures by serving as
222 chromatin loop anchors—a large fraction of which were found to be species-specific,
223 confirming TEs' role in genome innovation. Pioneering work in the last decade has extensively
224 outlined this contribution of TEs in shaping gene regulatory networks by depositing TF binding
225 sites in host genomes, leading to the origins of novel phenotypes like innate immunity and
226 pregnancy in mammals. Herein, lies the catch: research to date showcases the role of TEs in
227 bringing novelty and new regulatory functions to the host genome. Hence, TEs have long been
228 considered a source of genetic innovation. However, by comparing topologies instead of raw
229 DNA sequences in this study, for the first time, we have been able to reveal the role of TEs in
230 3D genome conservation. This seemingly counter-intuitive role of species-specific parasitic
231 sequences in helping maintain ancestral genome architecture is fundamentally different from
232 all current and previous work regarding TEs' role in gene regulation. This role is mediated by a
233 long-postulated, classic genetic phenomena of binding site turnover—for CTCF in this case.
234 Redundant TE-derived CTCF sites in the vicinity of conserved chromatin anchor/ boundary can
235 sometimes take over from the conserved anchor/boundary element, thus slightly shifting the
236 anchor/boundary site while largely maintaining the 3D structure. Certain TE subfamilies like
237 mouse SINE B2s contain pre-existing CTCF motifs within them, while others like mouse
238 RLTR30 provide sequence fodder which upon a couple of specific point mutations can acquire
239 CTCF binding and potentiate this binding site turnover.

240 In this study, 123 turnover events were observed in mouse on the basis of 3331
241 annotated loops (3.7%) whereas in humans 89 turnover events were observed out of 9448
242 loops (0.94%). This 4-fold higher rate of turnover events in mouse highlights differences in

243 between species and the turnover phenomenon being investigated. The higher rate of loop
244 anchor CTCF turnover in the mouse genome was amplified by the arrival of CTCF-motif
245 containing B2 elements. The genome is replete with such events and we have for the first time
246 functionally dissected and validated them in the context of 3D genome conservation, opening
247 the doors up for such investigations in the field for enhancer or promoter turnover events.

248 The *fons et origo* of CTCF motifs in B2 SINEs has been extensively researched. B2 SINEs
249 are derived from tRNA genes. Mouse tRNA genes have been shown to possess classical
250 insulator activity and the potential to function as boundary elements (*38*). Moreover, CTCF-
251 binding enrichment in B2 SINEs and repeat-driven dispersal of CTCF-binding has been shown
252 to be a fundamental, ancient, and still highly active mechanism of genome evolution in
253 mammalian lineages (*22*).

254 Similarly, the role CTCF motifs in viral genome regulation has been a topic of
255 tremendous interest and investigation. In EBV, this control involves direct binding of CTCF
256 across the viral genome and the formation of three-dimensional loops between virus
257 promoters and enhancers (*39*). CTCF has been shown to be important in the regulation of gene
258 expression of a number of human DNA viruses (*40*). CTCF also plays a critical role in epigenetic
259 regulation of viral gene expression to establish and/or maintain a form of latent infection that
260 can reactivate efficiently (*41*). Recent evidence has also shown that HTLV-1 inserts an ectopic
261 CTCF binding site forming loops between the provirus and host genome, altering expression of
262 proviral and host genes (*42*). CTCF has also been shown to promote HSV-1 lytic transcription
263 by facilitating the elongation of RNA Pol II and preventing silenced chromatin on the viral
264 genome (*43*). Moreover, one can speculate that having a CTCF motif can not only help in
265 maintaining viral genome confirmation but can also help insulate the chromatin activity of the
266 neighborhood wherein the virus inserts into the host genome. It may also increase the chances
267 of long-range interactions taking place which can sometimes bring in other TFs and/or
268 polymerase, leading to enhanced transcription at the site of viral integration.

269 Our in-depth analysis of 3D genome structures upon genetic manipulation of candidate
270 TEs revealed principles of how 3D genome evolves. In one example, a human TE provided a
271 conserved chromatin boundary and loop anchor, whereas the ancestral CTCF site had decayed.

272 Upon deletion, the chromatin domains collapsed, and loops eliminated, underscoring the
273 importance of the TE in maintaining the local 3D genome structure.

274 In another case where a human TE provided a similarly conserved boundary and loop
275 anchor, the ancestral CTCF site was still recognizable but was decommissioned. Deletion of the
276 TE resulted in reinstallation of the ancestral CTCF site to form a slightly shifted boundary and
277 loop anchor, and the local chromatin domains were largely preserved. In this second case that
278 we validated, we undid the events that took place during the course of (tens of millions of
279 years) evolution by removing a young TE (LTR41) and having the ancestral "decommissioned"
280 TE (MER82) re-uptake its function, thereby "reversing" the path of evolution in a dish (in days).
281 Thus, experimentally demonstrating the evolutionary impact of a TE-derived CTCF site.
282 Moreover, the concept of such shadow loop anchors residing in TEs that can be activated upon
283 escape from epigenetic silencing is extremely crucial to take into account for studies pertaining
284 to diseases of the epigenome like certain cancers, their treatment and therapy. This study also
285 underscores the redundancy that exists in the genome when it comes to CTCF binding sites
286 and can potentially explain why we may not always see a change in 3D genome structure upon
287 deleting CTCF binding sites.

288 It is important to remember that the contribution outlined in this manuscript are
289 underestimates as we have yet to (i) uniquely identify all loop anchor CTCF sites (especially in
290 highly repetitive regions), (ii) annotate all repetitive elements, especially ancient TEs that have
291 diverged far from their identity (*18*), and (iii) identify other architectural proteins and expand
292 this framework beyond just CTCF-derived loop anchors.

293 While most studies highlight TEs' role in innovating new functions by providing novel
294 regulatory elements such as enhancers and promoters, we implicate the role of TEs in
295 functional conservation inviting us to reexamine this unconventional role—perhaps many novel
296 regulatory elements derived from TEs are not creating new functions, but rather providing
297 redundant genetic material thus contributing to the robustness of gene regulatory networks.
298 These findings will undoubtedly stimulate investigations to explore the multitude modes of
299 regulatory evolution mediated by TEs. Indeed, recent evidence has linked the transcriptional

300 activation of retrotransposons to restructuring of genome architecture during human
301 cardiomyocyte development (44).
302 A major caveat of the analysis presented in this study is that the *in situ* Hi-C maps (re-
303 analyzed in this study) of the 9 cell lines were sequenced to varying depths, and thus differ in
304 their resolution and "completeness" of loop annotations. Hence, due to this limitation of
305 publicly available high-resolution HiC data, our findings likely represent a lower bound of TE's
306 involvement in shaping both the conserved and species-specific 3D genome. These analyses
307 need to be revisited as and when higher-resolution datasets are available.
308 Lastly, our study opens the doors for population-scale genetic variation studies that
309 identify polymorphic TE insertions to be reconciled with population-scale 3D genome and
310 regulatory variation. These future explorations will present yet another vignette of
311 transposable elements and their very many roles in accelerating adaptive evolution.
312
313 **CONCLUSIONS**
314 Taken together, our findings reveal a formerly uncharacterized role that TEs have
315 played in the evolution of higher-order chromosomal structures in mammals. TEs have
316 contributed a substantial number of loop anchors in mouse and human 3D genomes, a fraction
317 of which were co-opted to help maintain conserved higher-order chromosomal structures. TE
318 transposition provides redundant CTCF motifs and a novel method for CTCF binding site
319 turnover to maintain regulatory conservation (defined here as the preservation of long-range
320 chromosomal interactions, loop and boundary formation), by compensating for the loss of
321 local primary sequence—local sequence that would have otherwise allowed the assessment of
322 purifying selection. Deletion of these TEs in human cell lines eliminated the chromatin loops
323 that they anchor and resulted in collapse of conserved chromatin structure, as expected by our
324 hypothesis. More strikingly, we demonstrate that in another case the loop anchor shifted to an
325 alternative TE-derived CTCF site nearby, resulting in largely unchanged chromatin structure,
326 underscoring the dynamic nature and robustness of the 3D genome upon TE infiltration. These
327 TEs that maintain conserved chromatin loops via turnover are hypomethylated through deep
328 time, an observation that highlights the intimate interplay between genome, epigenome, and

329 3D genome in evolution. This research provides a foundation to study the impact of TEs and
330 expand our understanding of chromosomal folding—its emergence, maintenance and
331 transformation—in the context of evolving genomes. Ultimately, our study reveals how selfish
332 genetic elements, regardless of their origins, can be repurposed to provide redundant TF
333 motifs, maintain latent genome sanctity and regulatory fidelity by conserving 3D structure.
334
335 **FIGURE LEGENDS**
336 **Figure 1: Contribution of repetitive elements (REs) to chromatin loops in humans and**
337 **mouse.** (**A**) Pie charts representing percentage of loops and (**B**) unique loop anchor CTCF sites
338 derived from REs in a variety of human and mouse cell types. (**C**) Stacked bar plots showing the
339 distribution of RE-derived anchor CTCF across major RE classes in the various human and
340 mouse cell types. Stacked bar plots showcasing the distribution of RE-derived anchor CTCF vs.
341 background and CTCF ChIP peaks across (**D**) major RE classes and (**E**) major RE families in
342 matched blood lymphoblastoid cell line (mouse = CH12-LX; human = GM12878).
343
344 **Figure 2: Contribution of TEs in the conservation landscape of human and mouse loops.** (**A**)
345 Venn diagram representing the various classes of chromatin loops based on their orthology
346 and bar plots showing the contribution of REs to anchor CTCFs of each class of loops. (**B**) Age
347 distribution and age of individual TEs that contribute loop anchor CTCF sites (black dots for
348 orthologous loops; gold dots for non-orthologous loops) (left), total contribution to loop
349 anchor CTCF sites (middle), distribution of orthologous and non-orthologous loops (right)
350 derived from the top 13 TE subfamilies in mouse and (**C**) humans. Estimated primate/rodent
351 divergence time (82 million years ago) is from (Meredith et al, 2011). (**D**) Contact maps
352 representing a conserved chromatin loop in a syntenic region between human and mouse (**E**) A
353 MER20 transposon insertion provides a redundant CTCF motif that helps in maintaining the
354 conserved 3D structure via CTCF binding site turnover with remnants of the ancestral CTCF
355 motif, well conserved in most non-rodent mammals (Supplementary Figure 2), still seen in the
356 mouse genome.

357 **Figure 3: TEs are necessary for maintaining conserved higher-order chromosomal**
358 **structures in humans.** (**A**) Results of a CRISPR/Cas9-based deletion of an L1M3f element at
359 chr10:26–28 Mb in GM187278 cells. Mega-contact maps (details in Methods) generated using
360 Hi-C[2] technology for the (top) WT locus and (bottom) KO (ΔL1M3f) locus. (**B**) Virtual 4C plot
361 displaying total percent interactions emanating from an anchor on a 5kb-window containing
362 the L1M3f element. (**C**) Boxplot measuring the percent inter-domain interactions (Table S2.5)
363 across the targeted domain and a control domain (boundaries unaffected by CRISPR edits)
364 using subsampled contact maps (details in Methods). (**D**) Results of CRISPR/Cas9-based
365 deletion of an LTR41 element at chr8:70.3–71.8 Mb in GM187278 cells. Mega-contact maps
366 generated in Hi-C[2] experiments for the (top) WT locus and (bottom) KO (ΔLTR41) locus. (**E**)
367 Virtual 4C plot displaying total percent interactions emanating from an anchor on a 5kb-
368 window containing the left anchor CTCF of the conserved loop, and (**F**) the LTR41 element.

369 **Figure 4: Turnover TEs are hypomethylated through evolutionary time.** (**A**) Methylation
370 signature ±2kb around CTCF sites that help maintain orthologous loops segmented by the
371 origin of the anchor CTCF site (**B**) Methylation-associated and non-methylation mutational
372 signature of individual TEs relative to its ancestral sequence in humans (mouse TE data
373 available in Supplementary Figure 8). Alignments were performed using crossmatch (shown
374 here) and Needle (details in Methods, results in Supplementary Figure 9). Error bars show one
375 standard deviation of the means from 1000 simulations. (**C**) Schematic depicting the
376 framework of TE-mediated CTCF binding site turnover that highlights the intimate reciprocity
377 between the TE, genome and epigenome, to help maintain conserved 3D genome.

378 **REFERENCES**

379 1. SSP Rao et al., *Cell* **159**, 1665-1680 (2014).
380 2. Z Tang et al., *Cell* **163**, 1611-1627 (2015).
381 3. T Sexton et al., *Cell* **148**, 458-472 (2012).
382 4. JR Dixon et al., *Nature*. **485**, 376-380 (2012).
383 5. DU Gorkin et al., *Cell Stem Cell* **14**, 771-775 (2014).
384 6. W Schwarzer et al., *Nature* **551**, 51–56 (2017).
385 7. AR Strom et al., *Nature* **547**, 241–245 (2017).
386 8. AL Sanborn et al., *Proc Natl Acad Sci*. **112**, E6456-E6465. (2015).
387 9. G Fudenberg et al., *Cell Rep*. **15**, 2038–2049 (2016).
388 10. V Sundaram et al., *Genome Res*. **24**, 1963-1976 (2014).

11. G Bourque et al., *Genome Res*. **18**, 1752-1762 (2008).
12. G Kunarso et al. *Nat Genet*. **42**, 631-634 (2010).
13. PÉ Jacques et al., *PLoS Genet*. **9**(5) (2013).
14. T Wang et al., *Proc Natl Acad Sci*. **104**, 18613-18618 (2007).
15. EB Chuong et al., *Science* **351**, 1083-1087 (2016).
16. VJ Lynch et al., *Nat Genet* **43**, 1154-1159 (2011).
17. BJ Britten, EH Davidson. *Q Rev Biol*. **46**, 111-138 (1971).
18. APJ de Koning et al., *PLoS Genet*. **7** (2011).
19. AS Hinrichs, *Nucleic Acids Res*. **34**, 590-598 (2006).
20. C Feschotte, EJ Pritham. *Annu Rev Genet*. **41**, 331-368 (2007).
21. V Sundaram, T Wang. *BioEssays*. **40**, 1700155 (2018).
22. D Schmidt et al., *Cell* **148**, 335-348 (2012).
23. MZ Ludwig et al., *Development* **12**, 3325–3330 (1998).
24. AM Moses et al., *PLoS Comput Biol*. **2**, 130 (2006).
25. S Venkataram, JC Fay. *Genome Biol Evol*. **2**, 851–858 (2010).
26. D Villar et al., *Nat Rev Genet*. **15**, 221-233 (2014).
27. MA Matzke et al., *Plant Mol Biol*. **43**, 401-415 (2000).
28. JA Yoder et al., *Trends Genet*. **13**, 335-340 (1997).
29. RK Slotkin et al., *Nat Rev Genet*. **8**, 272-285 (2007).
30. A Huda et al., *Mob DNA* **1**, 2-12 (2010).
31. CB Lowe, D Haussler. *PLoS One* **7**, 43128 (2012).
32. G Bejerano et al., *Nature* **441**, 87–90 (2006).
33. MG Kidwell, DR Lisch. *Trends Ecol Evol*. **15**, 95-99 (2000).
34. C Kanduri et al., *Curr Biol*. **10**, 853-856 (2000).
35. S Kurukuti et al., *Proc Natl Acad Sci*. **103**, 10684-10689 (2006).
36. JC Shen et al., *Nucleic Acids Res*. **22**, 972-976 (1994).
37. AP Bird. *Nucleic Acids Res*. **8**, 1499–1504 (1980).
38. T Ebersole et al. *Cell Cycle*. **10**, 2779–2791 (2011).
39. I Tempera et al. *PLoS Pathog* **7**:e1002180 (2011).
40. I Pentland et al. *Viruses* **7**:3574-85 (2015).
41. JS Lee et al. *mBio* **9**:e02372-17 (2018).
42. Y Satou et al. *Proc Natl Acad Sci*. **113**(11):3054-3059 (2016).
43. F Lang et al. *Sci. Rep.* **7**, 39861 (2017).
44. Y Zhang, T Li, S Preissl et al., *biorXiv*. (2018).
45. RW Meredith et al., *Science* **334**, 521-524 (2011).
46. RH Waterston et al., *Nature* **420**, 520-562 (2002).
47. M Haeussler et al., *Genome Biol.* **17**, 148 (2016).
48. MA Moreno-Mateos et al., *Nature Methods* **12**, 982-988 (2015).
49. W Bao et al., *Mob DNA* **6**, 11 (2015).
50. A Smit et al., RepeatMasker Open-4.0.6 2013-2015. (2017).
51. P Rice et al., *Trends Genet.* **16**, 276-277 (2000).

METHODS

433 Dataset GEO accession numbers:

434 The genomic data analyzed in this study were obtained from publicly available
435 datasets. HiC datasets were obtained from GSE63525 (mouse: CH12; humans: GM12878, HeLa,
436 HMEC, IMR90, K562, NHEK). GM12878 ChIA-PET dataset was obtained from GSE72816.
437 GM12878 CTCF ChIP-seq datasets were obtained from ENCODE (ENCSR000AKB and
438 ENCSR000DZN). CH12 CTCF ChIP-seq datasets were obtained from Mouse ENCODE
439 (ENCSR000ERM and ENCSR000DIU). WGBS methylation dataset for GM12878 was also
440 obtained from ENCODE, GEO: GSE86765 (ENCSR890UQO). Mouse ESC and NSC HiC data was
441 obtained from PMID: 30414923.

442

443 Loop anchor CTCF–RE intersection:

444 We generated a list of unique anchor CTCF sites using the HiCCUPS output[1] for various
445 mentioned cell lines. We then overlapped loop anchor CTCF motifs identified using HiCCUPS
446 (*1)* with *RepeatMasker* (RMSK v4.0.7, for hg19 and mm9) and required at least 10bp of the core
447 CTCF motif to intersect with a repetitive element (RE) to call it a RE-derived loop anchor CTCF
448 site. Further, only loops with (i) at least one known RE-derived anchor CTCF site, or (ii) two
449 non-RE derived anchor CTCF sites were taken into consideration for analysis of RE-derived
450 loop counts, because we can definitively say whether the loops and their loop anchor CTCF
451 sites were derived from REs or not. Loops with both unidentified loop anchor CTCF sites, or
452 one unidentified and one non-RE derived anchor CTCF site were not considered as there is the
453 possibility of having at least one of the other anchor CTCF sites derived from a RE. We followed
454 the same methodology when considering ChIA-PET loops.

455

456 TE class and family distribution

457 We ran RepeatMasker v4.0.7 with the -s slow search parameter on the hg19 and mm9
458 genomes to obtain a comprehensive list of REs in the genome and their corresponding
459 subfamily, family and class annotations. We used RE counts (generated as previously outlined)
460 to characterize their distribution to loop anchor CTCF sites. For characterizing RE-derived
461 CTCF binding peaks, we repurposed a previously used strategy (*10*). Briefly, we required that
462 the centers of the MACS-called peaks of ENCODE-generated CTCF ChIP datasets overlapped
463 with RE fragments. We used the length distribution of various RE family and classes in the
464 entire genome as the background distribution.

465

466 Loop orthology check:

467 We used liftOver (*19*) to convert CH12 loop annotations from mm9 mouse genome
468 coordinates to hg19 human genome coordinates. We used various sequence match rates
469 (minMatch = 0.05, 0.1..., 1) to convert CH12 mouse peaks from mm9 genome coordinates to
470 hg19 genome coordinates. To optimize for the minMatch parameter, we generated ten

shuffled (randomized) peak annotations by using bedtools shuffle –chrom command to permute their location on the chromosome of origin. minMatch parameter of 0.1 was chosen for liftOver analyses henceforth, as it resulted in the greatest number of features being lifted over (on average) and lower coefficient of variation across the 10 simulated sets. We lifted over 3245 out of 3331 mouse peaks from mm9 to hg19, using the minMatch 0.1, to facilitate cross-species peak annotations comparison. To call a mouse feature conserved in humans, we required that the loop anchor pairs individually lie within a min(half of loop length, vicinity threshold) window of an existing loop anchor pair. The vicinity threshold was put in place to account for cross-species liftOver errors and facilitate comparison of higher-order chromosomal features that vary from 120Kb to 125Mb in length (in mouse). We tested multiple vicinity thresholds ranging from 500bp to 100Mb and identified false discovery rates using simulated sets of mouse features and comparing them to the orthology observed between the real CH12 (mouse) and GM12878 (human) features. We decided to use 50kb as the vicinity threshold as it corresponded to a false discovery less than 0.1. We found that 1688 CH12 mouse peaks overlapped at least one corresponding peak in GM12878 human lymphoblastoid cells. We performed a similar analysis to compare 'muranized' human features (liftOver from GM12878) to actual mouse features (CH12). We found that 1900 GM12878 human peaks overlapped at least one corresponding peak in CH12 mouse lymphoblastoid cells. We then filtered for features that displayed reciprocal matches (reciprocal best hits) in the two comparisons (mouse-to-human and human-to-mouse) as stated above. Finally, we curated the list by considering genic, epigenomic and transcriptomic synteny to pick exactly one orthologous human loop to a corresponding mouse loop, to enlist 1596 high-confidence orthologous peak calls (Table S1.1). A brief flowchart of the pipeline is shown below:

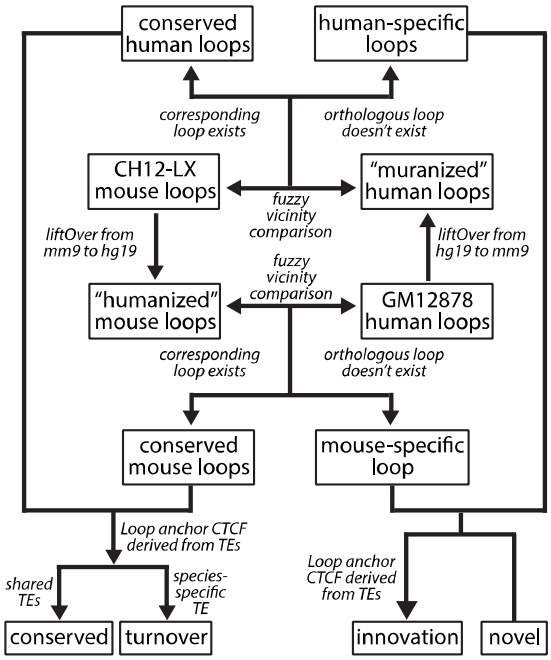

496 TE age estimation:

497 Species divergence times were based on (*45*). Repeat ages were estimated by dividing
498 the percent divergence of extant copies from the consensus sequence by the species neutral
499 substitution rate. Substitution rates (mutations/yr) used were as follows: humans: $2.2x10^{-9}$;
500 mouse: $4.5x10^{-9}$, from (*46*). Jukes-Cantor and Kimura distances were calculated by aligning
501 each TE to its consensus sequence and counting all possible mutations (see below). Single
502 nucleotide substitution counts were normalized by the length of the genomic TE minus the
503 number of insertions (gaps in the consensus). These mutation rates were then used to calculate
504 the Jukes-Cantor and Kimura distances for each genomic TE.

505

506 Candidate selection and filtering:

507 After manually curating the list of conserved loops, we looked for TE-derived
508 orthologous loops in humans that were discordant for TEs in mouse. After identifying the list
509 of TE-derived CTCF turnover events in humans, we comprehensively surveyed the local CTCF
510 binding landscape (CTCF ChIP-seq peaks) to ensure (i) there weren't other CTCF binding sites
511 in the vicinity that could function as loop anchors in humans (in the first case); and (ii) there
512 was only one other unique CTCF binding site, i.e. the ancestral CTCF motif (in the second case).
513 We also ensured that the TE insertion from which the loop anchor CTCF site was derived was
514 human-specific and not present in mouse (Table S1.2). We repeated this analysis to identify
515 TE-mediated turnover in mouse as well (Table S1.3). We also identified events wherein TEs
516 mediated turnover events both in mouse as well as human (Table S1.4). One possible
517 explanation for this observation is that similar selective pressures (i.e. the need to maintain
518 higher-order chromosomal structure) led to the convergent co-option of species-specific TEs
519 at syntenic locus, independently in both the genomes.

520

521 Cell culture methods:

522 GM12878 cell lines were grown between 200K-800K cells/ml in 10ml cultures in T-25
523 flasks, in a humidified incubator with 95% CO_2 at 37°C in RPMI1640 media (Gibco, 1187-085)
524 supplemented with 15% fetal bovine serum (Corning, 35-011-CV) and 100U/ml penicillin-
525 streptomycin (Gibco, 15140-122) as per the ENCODE standards.

526

527 CRISPR-Cas9 mediated genome engineering:

528 Our CRISPR workflow consisted of the following steps: We identified turned over
529 chromatin loops that are maintained by TEs, with unique, correctly oriented TE-derived CTCF
530 motifs within loop anchors (*1*). We used two independent CRISPR sgRNA design engines
531 CRISPOR (*47*) and CRISPRScan (*48*) to rationally design multiple pairs of sgRNAs that have
532 high cutting efficiency and minimizing off-target effects. We used pU6-(BbsI)_CBh-Cas9-T2A-
533 BFP plasmid (Addgene, 64323) and pU6-(BbsI)_CBh-Cas9-T2A-mCherry plasmid (Addgene,

534 64324) as the CRISPR delivery vectors. For each sgRNA, we designed and annealed two single-
535 stranded oligos with compatible overhangs that can be cloned into BbsI-digested BFP and
536 mCherry CRISPR vectors through standard ligation techniques. For every pair of sgRNAs, we
537 constructed BFP-CRISPR vectors and mCherry-CRISPR vectors that express sgRNAs targeting
538 upstream and downstream of the candidate TEs, respectively. BFP-CRISPR vectors and
539 mCherry-CRISPR vectors each were co-transfected into GM12878 cells in antibiotic-free media
540 using the Neon transfection system. After 24 hours of incubation, the transfected cells were
541 analyzed by flow-cytometry (Beckman Coulter MoFlo) for BFP-positive and mCherry-positive
542 subpopulations. Transfection efficiencies were usually between 3-5%. We single-cell sorted
543 these double-positive fluorescent cells into 96-well plates for clone expansion and allowed to
544 grow for 21-28 days. After that, 20-48 clones were screened per transfection. Genomic DNA
545 from CRISPR clones was extracted using *Quick-DNA* Miniprep kit for genotyping and validated
546 with Sanger sequencing. Details of sequences used to generate clones used in this study are
547 listed in Table S2.4. We then performed *in situ* Hi-C on the selected mutated cell lines and
548 performed hybrid selection on the in situ Hi-C libraries for a region around the targeted TE to
549 generate Hi-C^2 libraries that can easily and cheaply be sequenced to read off the effects of our
550 TE deletions on local genome folding.
551
552 Hi-C^2 probe design:
553 To design probes targeting the two regions for HYbrid Capture Hi-C (Hi-C^2), we
554 followed a similar approach as (*8*). In short, we (i) identified all MboI restriction sites within the
555 target region, (ii) we designed our bait probe sequences to target sequences within a certain
556 distance of the MboI restriction sites as Hi-C ligation junctions occur between them, (iii) we
557 followed a similar three-pass probe design strategy sequentially increasing various parameters
558 like the distance of the probe from the MboI restriction site, the number of repetitive bases,
559 the GC content, probe density in gaps with relaxed probe design quality filters. We then
560 removed overlapping probes or probes with identical sequences. After all three passes, we
561 identified 2741 unique probes covering region 1 (chr10:26-28Mb; 1.37 probes/kb) and 1856
562 probes covering region 2 (chr8:70.3-71.8Mb; 1.24 probes/kb). 15bp primer sequences (unique
563 for each region, details in Table S2.3) were then appended to both ends of the 120bp probe
564 sequence to facilitate single oligo pool synthesis and subsequent amplification of region-
565 specific sub-pools. Probe construction and hybrid selection was then followed with sequences
566 specific to this study using the same strategy detailed in (*8*).
567
568 Hi-C experiments:
569 The Hi-C datasets used in our analyses were generated using the *in situ* Hi-C protocol
570 standardized by the 4DN consortia. In brief, the in situ Hi-C protocol involves crosslinking cells
571 with 1% formaldehyde for 10 minutes, permeabilizing them with nuclei intact, digesting the

572 DNA with MboI (4-cutter restriction enzyme), filling the 5'-overhangs while incorporating
573 biotin-14-dATP (a biotinylated nucleotide), followed by ligating the resulting blunt-end
574 fragments, shearing the DNA to a 400-700bp fragment size, capturing the biotinylated ligation
575 junctions with streptavidin beads, building an Illumina library with 10-12 rounds of PCR
576 amplification, and finally analyzing the resulting fragments with paired-end sequencing. The
577 resulting library was always shallow sequenced to 500K-4M reads to check for library build
578 quality looking at key statistics such as complexity, number of Hi-C contacts, inter vs.
579 intrachromosomal interactions, and long-range vs/ short-range intrachromosomal
580 interactions. Libraries that passed the quality check were either sequenced deeper and/or used
581 as pools for subsequent Hi-C^2 experiments.
582 For our genome engineering experiments, we generated 14 in situ Hi-C libraries (Table
583 S2.1) from GM12878 cells. We also generated 16 *in situ* Hi-C^2 libraries from various genome-
584 engineered GM12878 cell lines on which we performed hybrid selection. All *in situ* Hi-C libraries
585 generated as part of this study are detailed in Table S2.2. All the Hi-C data was processed using
586 the computational pipeline described in full detail in (*1*). Hi-C libraries were sequenced to a
587 depth of between 624K-333M reads (on average, 63.8M reads). Hi-C^2 libraries were sequenced
588 to a depth of between 6.7M-168M reads (on average, 35.8M reads). All data was initially
589 processed using the pipeline published in (*1*) and visualized on the desktop and web version of
590 Juicebox. We combined Hi-C and Hi-C^2 contact maps corresponding to the same genotype and
591 the same locus using the Juicer's mega.sh script as these are in essence "biological" replicates,
592 to generate higher resolution megamaps.
593
594 <u>Analysis of cross-domain interactions:</u>
595 We subsampled the Hi-C^2 corresponding to the R1-WT megamap (containing 46M
596 reads) and R1-KO (containing 56M reads) for 5M reads, 10 times to create 10 independent R1-
597 WT and R1-KO mini-maps. For each of these HiC maps, we used the Juicer Tools `dump`
598 command to extract the raw contact matrix. Intradomain interactions were defined as
599 interaction that (i) originate and terminate in domain 1, or (ii) originate and terminate in
600 domain 2. Interdomain interactions were defined as interactions that originate in domain 1 and
601 terminate in domain 2. We then calculate percentage of cross-domain interactions for each of
602 the mini-maps using the formula: (number of intradomain-interactions)*100 / ((number of
603 intradomain-interactions) + (number of interdomain-interactions)). The percentage of cross-
604 domain interactions were calculated for the target domain as well as a control domain. The
605 distribution of cross-domain interactions across the targeted domain was found to be
606 significantly different in the KO vs. the WT (t-Test: Two-Sample Assuming Unequal Variances,
607 p-value = 1.40668×10^{-16}). The distribution of cross-domain interactions across a nearby control
608 domain however was not found to be significantly different in the KO vs. the WT (t-Test: Two-

609 Sample Assuming Unequal Variances, p-value = 0.013254165). Raw simulation data and
610 statistics are provided in Table S2.5.
611 For Figure S3C, we used the Hi-C megamap corresponding to R2-WT and R2-KO to
612 retrieve raw interaction counts at a 100kb resolution. Percent cross-domain interactions was
613 calculated using the formula stated above. We calculated the enrichment of cross-domain
614 interactions in the LTR41-DKO w.r.t. the WT across the targeted domain as well as a nearby
615 control domain.
616
617 DNA Methylation analysis:
618 We generated a methylation metaplot representing the mean CpG methylation value
619 from WGBS data (ENCODE dataset: ENCFF835NTC) of 20bp sliding windows, centered on
620 CTCF motifs (and ±2kb around it) segmented by their origin/TE-derivation status.
621
622 Analysis of TE Mutational Profile:
623 1. TE consensus construction
624 For most of the TE subfamilies, we retrieved the consensus sequences from the
625 RepBase library (RepBase 22.02, RepeatMaskerEdition20170127) (*49*). However, LINE
626 elements are fragmented to 5' end, ORF2 and 3' end regions in RepBase library. To reconstruct
627 full-length LINE consensus, we identified TE fragments in human and mouse genome using
628 RepeatMasker and compared the standard output (.out file) with the alignment output (.align
629 file) from the same RepeatMasker run (*50*). For each LINE element in the standard output, we
630 summarized which 5' end, ORF2, and 3' end fragments have been used most to construct the
631 full-length element. Then we use EMBOSS Water local alignment algorithm to align the three
632 pieces together and generated the full-length LINE consensus sequences (*51*).
633 2. Crossmatch alignments
634 We ran RepeatMasker 4.0.7 on the mm9 and hg19 genomes using crossmatch as the
635 search engine. We then parsed the alignment file to determine the substitution rates between
636 the ancestral sequence and the genomic element. For each genomic element, we counted the
637 number of A-to-C, A-to-G, A-to-T, C-to-A, C-to-G, C-to-T, G-to-A, G-to-C, G-to-T, T-to-A, T-
638 to-C, and T-to-G substitutions (single nucleotide substitutions), where the first nucleotide
639 indicates the ancestral sequence and the second nucleotide indicates the genomic sequence.
640 We ignored any substitutions that involved ambiguous nucleotides. We also counted the
641 number of insertions and deletions. All substitution frequencies were normalized by the length
642 of the genomic sequence to estimate the substitution rates in each TE. Any genomic TE with a
643 length less than 20% of the ancestral sequence was filtered out. For each single nucleotide
644 substitution, we calculated the average substitution rate in two subsets of TEs (details below).
645 We also calculated the combined C-to-T and G-to-A substitution rate (methylation-associated
646 substitutions) and the combined rate of all other substitutions (non-methylation-associated

substitutions) to compare the rate of DNA methylation-induced mutations to other mutations. The methylation substitution rate was computed by taking the average of the C-to-T and G-to-A rates for each TE and then averaging over turnover events. The non-methylation substitution rate was computed by taking the average of all other (ten) single nucleotide substitutions for each TE and then averaging over turnover events.

We generated a background distribution by repeating this analysis on 1000 permutations of all genomic TEs. We first calculated the frequency of each TE subfamily in the set of turnover events. For each permutation, we randomly selected genomic TEs (not involved in anchoring loops) from each subfamily to reflect their frequency in turnover events. The single nucleotide substitution rate, methylation-associated substitution rate, and non-methylation-associated substitution rate were calculated as described above. The distribution of all substitution rates from the permutations follow a normal distribution (KS test, $P > 0.0036$, Bonferroni correction alpha = 0.05 for N = 14 hypotheses, Supplemental Table S3.1). The background distribution was then used to perform a left-tailed z-test. We did not compute a two-tailed p-value because our null hypothesis is that the observed mutation rates are greater than or equal to the background distribution mean. For the 12 single nucleotide substitutions, we used Bonferroni correction to account for multiple hypotheses.

3. Needle realignments

RepeatMasker performs post-processing after running crossmatch, so coordinates and TE subfamily assignments in the .out file do not always reflect the contents of the .align file. To improve our estimates of mutation rates, we realigned each TE to its matched consensus sequences. We extracted the genomic and subfamily consensus sequence using the coordinates reported in the .out file. We then performed a global alignment using EMBOSS Needle v6.6.0.0 using a gap open penalty of 10, a gap extension penalty of 0.5, and the EDNAFULL scoring matrix. We used the alignment to recompute single nucleotide substitutions for each TE and then repeated the same analysis we used for crossmatch alignments. We did not filter out TEs with a length less than 20% of the ancestral sequence because this filter was originally put in place to account for discrepancies between the .align and .out files. As before, the distribution of all substitution rates from the permutations follow a normal distribution (KS test, $P > 0.0036$, Bonferroni correction alpha = 0.05 for N = 14 hypotheses, Supplemental Table S3.2).

DECLARATIONS

Ethics approval and consent to participate Not applicable

Consent for publication Not applicable.

Availability of data and material The data sets generated and analyzed in this current study will be uploaded to GEO upon acceptance

Competing Interests Authors declare no competing interests.

Funding M.N.K.C. was partly supported by the Precision Medicine Pathway, Washington University; H.S.J. was partly supported by NIH grant T32 GM007067; X.Z. was partly supported by R25DA027995; T.W. is supported by R01HG007175, U01CA200060, U24ES026699, U01HG009391, U41HG010972 and American Cancer Society RSG-14-049-01-DMC.

Authors' Contributions M.N.K.C. and T.W. conceived and designed this study; M.N.K.C. analyzed the data, performed experiments, generated sequencing libraries, and wrote the manuscript with inputs from T.W.; R.Z.F., J.T.W., and X.Z. contributed text and revised the manuscript; H.S.J. contributed reagents and resources; R.Z.F performed mutation frequency simulations along with M.N.K.C.; X.Z. generated TE ancestral sequences and TE alignments; T.W. supervised the project. All authors subsequently edited and approved the final manuscript.

Acknowledgements We thank members of the Wang Lab for helpful discussions related to the project; Jessica Hoisington-López and Maria Lynn Jaeger from The Edison Family Center for Genome Sciences & Systems Biology for assistance with sequencing; Matthew Patana & Daniel Schweppe from the Siteman Flow Cytometry core for FACS expertise.

Corresponding Author Correspondence and requests for materials should be addressed to Ting Wang.

Supplementary Materials

Table S1 – S3

Supplementary Figure 1 – 9

FIGURE 1

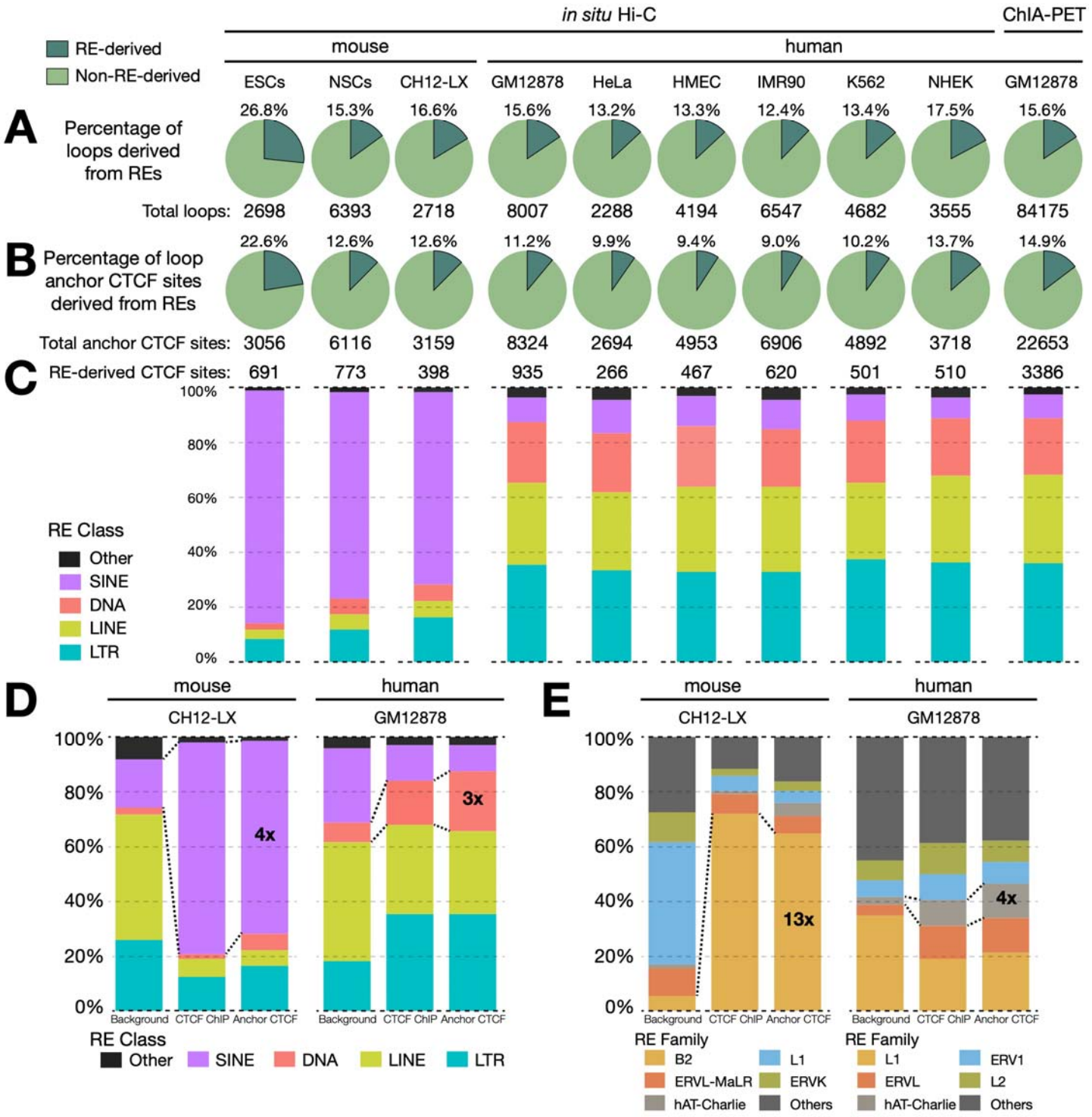
in situ Hi-C
ChIA-PET
RE-derived
Non-RE-derived
mouse
human
ESCs
NSCs
CH12-LX
GM12878
HeLa
HMEC
IMR90
K562
NHEK
GM12878
A
Percentage of loops derived from REs
26.8%
15.3%
16.6%
15.6%
13.2%
13.3%
12.4%
13.4%
17.5%
15.6%
Total loops: 2698 6393 2718 8007 2288 4194 6547 4682 3555 84175
B
Percentage of loop anchor CTCF sites derived from REs
22.6%
12.6%
12.6%
11.2%
9.9%
9.4%
9.0%
10.2%
13.7%
14.9%
Total anchor CTCF sites: 3056 6116 3159 8324 2694 4953 6906 4892 3718 22653
C
RE-derived CTCF sites: 691 773 398 935 266 467 620 501 510 3386
100%
80%
60%
40%
20%
0%
RE Class
Other
SINE
DNA
LINE
LTR
D
mouse
human
CH12-LX
GM12878
4x
3x
Background
CTCF ChIP
Anchor CTCF
RE Class
Other
SINE
DNA
LINE
LTR
E
mouse
human
CH12-LX
GM12878
13x
4x
RE Family
B2
L1
ERVL-MaLR
ERVK
hAT-Charlie
Others
L1
ERV1
ERVL
L2
hAT-Charlie
Others

FIGURE 2

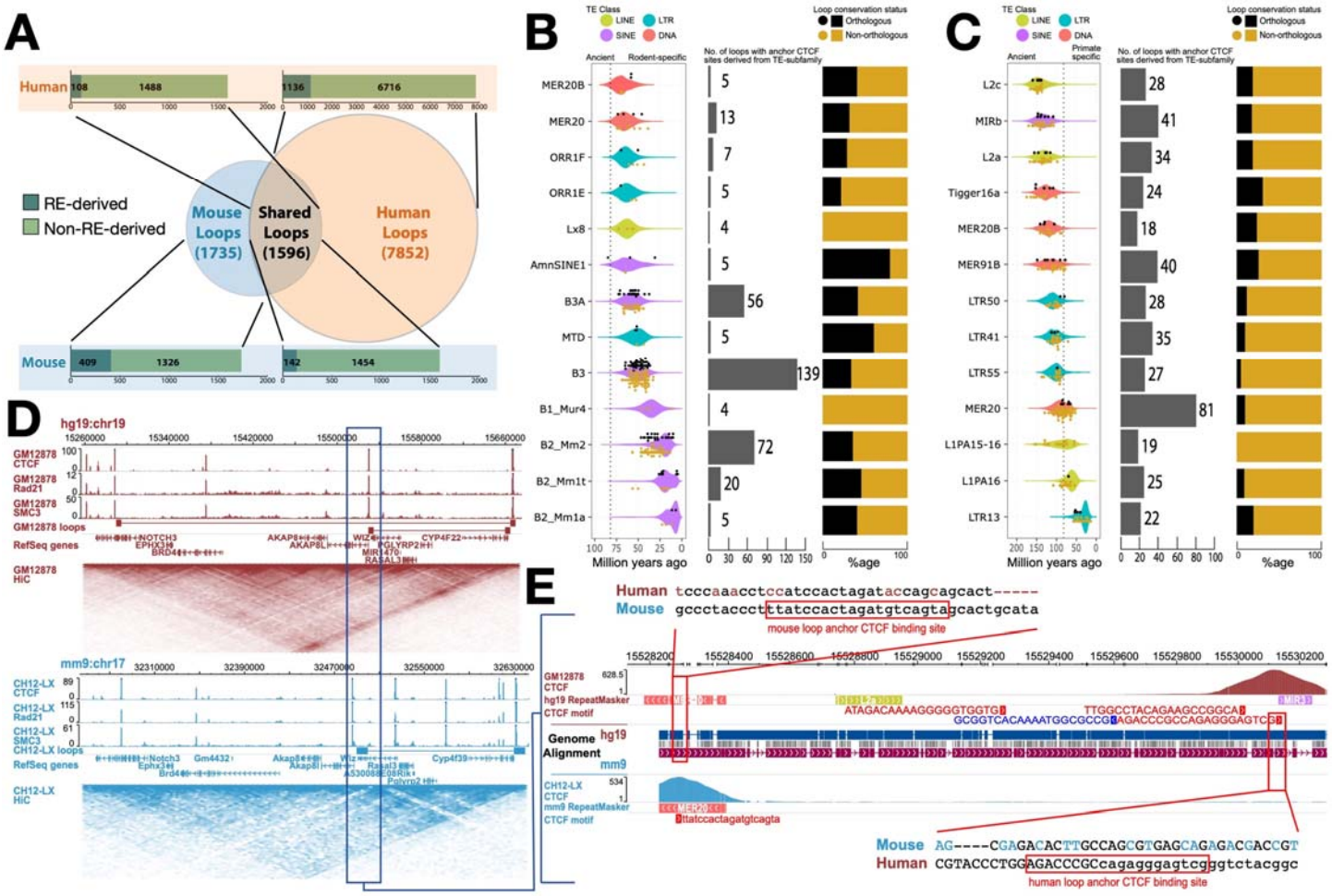
A
Human
108
1488
1136
6716
RE-derived
Non-RE-derived
Mouse Loops (1735)
Shared Loops (1596)
Human Loops (7852)
Mouse
409
1326
142
1454
B
TE Class
LINE
LTR
SINE
DNA
Ancient
Rodent-specific
No. of loops with anchor CTCF sites derived from TE-subfamily
Loop conservation status
Orthologous
Non-orthologous
MER20B
MER20
ORR1F
ORR1E
Lx8
AmnSINE1
B3A
MTD
B3
B1_Mur4
B2_Mm2
B2_Mm1t
B2_Mm1a
5
13
7
5
4
5
56
5
139
4
72
20
5
Million years ago
%age
C
Primate specific
L2c
MIRb
L2a
Tigger16a
MER20B
MER91B
LTR50
LTR41
LTR55
MER20
L1PA15-16
L1PA16
LTR13
28
41
34
24
18
40
28
35
27
81
19
25
22
D
hg19:chr19
GM12878 CTCF
GM12878 Rad21
GM12878 SMC3
GM12878 loops
RefSeq genes
GM12878 HiC
mm9:chr17
CH12-LX CTCF
CH12-LX Rad21
CH12-LX SMC3
CH12-LX loops
CH12-LX HiC
E
Human tcccaaacctccatccactagataccagcagcact-----
Mouse gccctaccctttatccactagatgtcagtagcactgcata
mouse loop anchor CTCF binding site
GM12878 CTCF
hg19 RepeatMasker
CTCF motif
Genome Alignment
hg19
mm9
CH12-LX CTCF
mm9 RepeatMasker
Mouse AG----CGAGACACTTGCCAGCGTGAGCAGAGACGACCGT
Human CGTACCCTGGAGACCCGCcagagggagtcggtctacggc
human loop anchor CTCF binding site

FIGURE 3

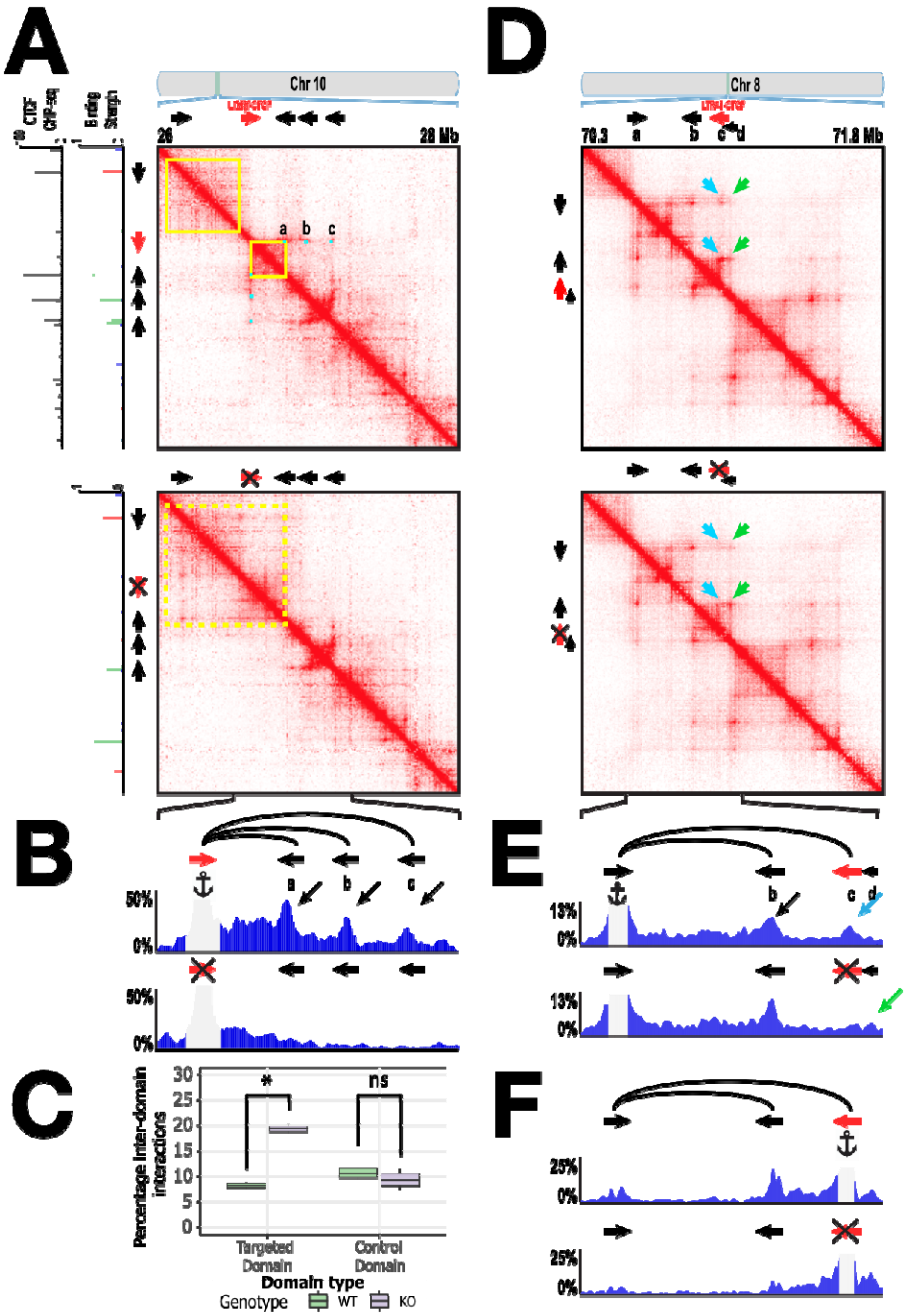
A
Chr 10
26
28 Mb
a b c
B
50%
0%
C
Percentage inter-domain interactions
30
25
20
15
10
5
0
*
ns
Targeted Domain
Control Domain
Domain type
Genotype
WT
KO
D
Chr 8
70.3
71.8 Mb
a b c d
E
13%
0%
F
25%
0%

FIGURE 4

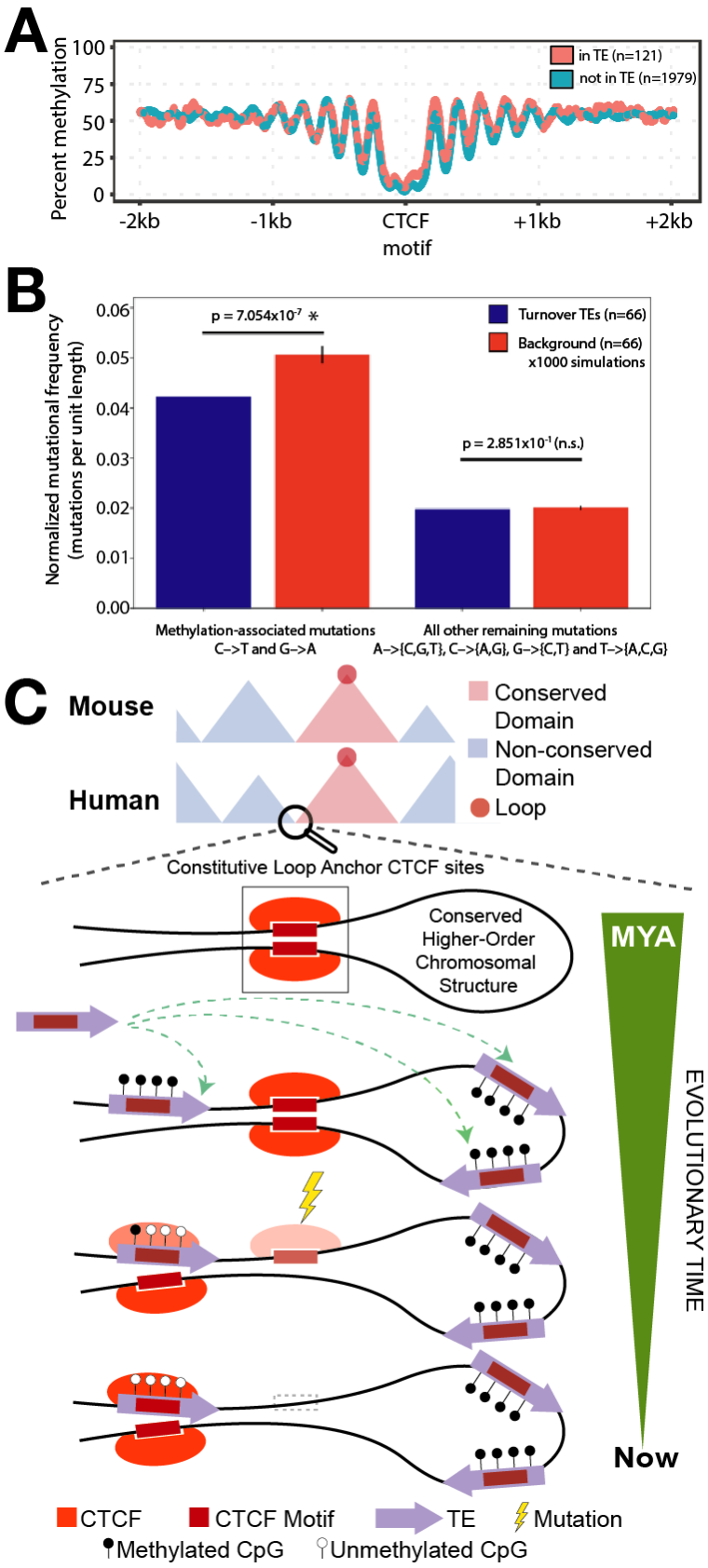
A
Percent methylation
100
75
50
25
0
in TE (n=121)
not in TE (n=1979)
-2kb
-1kb
CTCF motif
+1kb
+2kb
B
Normalized mutational frequency (mutations per unit length)
0.06
0.05
0.04
0.03
0.02
0.01
0.00
p = 7.054x10-7 *
Turnover TEs (n=66)
Background (n=66) x1000 simulations
p = 2.851x10-1 (n.s.)
Methylation-associated mutations C->T and G->A
All other remaining mutations A->{C,G,T}, C->{A,G}, G->{C,T} and T->{A,C,G}
C
Mouse
Human
Conserved Domain
Non-conserved Domain
Loop
Constitutive Loop Anchor CTCF sites
Conserved Higher-Order Chromosomal Structure
MYA
EVOLUTIONARY TIME
Now
CTCF
CTCF Motif
TE
Mutation
Methylated CpG
Unmethylated CpG